

Dynamic states of cells adhering in shear flow: From slipping to rolling

C. B. Korn and U. S. Schwarz

University of Heidelberg, Bioquant, BQ 0013 BIOMS Schwarz, Im Neuenheimer Feld 267, D-69120 Heidelberg, Germany

(Received 9 November 2007; published 10 April 2008)

Motivated by rolling adhesion of white blood cells in the vasculature, we study how cells move in linear shear flow above a wall to which they can adhere via specific receptor-ligand bonds. Our computer simulations are based on a Langevin equation accounting for hydrodynamic interactions, thermal fluctuations, and adhesive interactions. In contrast to earlier approaches, our model not only includes stochastic rules for the formation and rupture of bonds, but also fully resolves both receptor and ligand positions. We identify five different dynamic states of motion in regard to the translational and angular velocities of the cell. The transitions between the different states are mapped out in a dynamic state diagram as a function of the rates for bond formation and rupture. For example, as the cell starts to adhere under the action of bonds, its translational and angular velocities become synchronized and the dynamic state changes from slipping to rolling. We also investigate the effect of nonmolecular parameters. In particular, we find that an increase in viscosity of the medium leads to a characteristic expansion of the region of stable rolling to the expense of the region of firm adhesion, but not to the expense of the regions of free or transient motion. Our results can be used in an inverse approach to determine single bond parameters from flow chamber data on rolling adhesion.

DOI: [10.1103/PhysRevE.77.041904](https://doi.org/10.1103/PhysRevE.77.041904)

PACS number(s): 87.17.Aa, 83.10.Mj, 82.39.-k

I. INTRODUCTION

Rolling adhesion of white blood cells (leukocytes) along the vascular endothelium plays a key role in the immune response and is a prominent example for the interplay between transport and specific adhesion in biological systems [1–3]. Random encounters between cell and vessel wall lead to the formation of initial bonds based on adhesion receptors from the selectin family. Because selectins are characterized by fast association and dissociation kinetics, new bonds are readily formed on the downstream side and old bonds are continuously ruptured at the upstream side. If the processes of bond formation and rupture are sufficiently balanced, rolling adhesion results. As rolling velocity is smaller than the velocity of a cell moving freely in hydrodynamic flow, this mechanism allows the leukocytes to more efficiently survey the vessel wall for appropriate molecular signals. The main signals in this context are chemokine molecules, which indicate the presence of an infection and lead to firm adhesion based on the adhesion receptors from the integrin family. Firm adhesion in turn is a prerequisite for transendothelial migration into the surrounding tissue. Similar mechanisms are used by stem and cancer cells to disseminate in the body through the blood flow.

The main tool for investigating rolling adhesion under controlled conditions are flow chambers [4]. There receptor-carrying cells suspended in an aqueous solution are perfused in linear shear flow above a ligand-coated wall. For example, it was shown with flow chamber experiments that selectin bonds have fast kinetic rates and that the dissociation rate increases with force (slip bond), thus explaining their superior function in mediating rolling adhesion [5,6]. Recently it was demonstrated by a combination of atomic force microscopy and flow chamber experiments that the lifetime of single selectin bonds shows a biphasic response under force [7,8]. Such a catch-slip bond behavior might have evolved to avoid adhesion of leukocytes under static conditions. Indeed it has been found early in flow chamber experiments that leukocytes adhere only above a critical threshold of shear

[9]. In addition to specific properties of the molecular bonds, transport processes might also play an important role in creating the shear threshold [10,11]. Both rolling adhesion [12] and the shear threshold [13] have also been demonstrated in cell-free flow chamber experiments with ligand-coated micron-sized beads. Although cell-free rolling is more erratic than leukocyte rolling, this indicates that cellular features (such as cell deformability) are not essential to rolling adhesion. Flow chamber experiments also allow to study the exact effect of nonmolecular parameters, for example, of changes in the viscosity of the medium. By adding an inert substance such as the sugar ficoll, it is possible to change shear stress but not shear rate in a flow chamber experiment, thus dissecting the respective roles of force and transport [10,11,14].

The standard observable in flow chamber experiments is the translational velocity as a function of time [6,15,16]. From this time series further variables can be derived, for example average and standard deviation of velocity. In the case of low ligand density, a stopped cell is most likely held by a single bond and detaches without rebinding. Then the time series can be used to measure single bond lifetime. At higher ligand density, rolling occurs. Because rolling is never smooth but erratic due to the stochastic processes on the molecular level, then the time series can be used to measure pause time distributions. The velocity time series can also be used to define different states of motion of the cell. Typically a cell is said to undergo rolling whenever its mean velocity (averaged over some seconds) significantly decreases compared to the free (hydrodynamic) velocity. If no motion can be detected for several seconds, the cell is considered to be in firm adhesion [16].

Because rolling adhesion is not only of large physiological importance, but also characterized by an intricate interplay of different physical factors, it has long been subject to intense modeling efforts. If molecular effects are of interest, then such modeling efforts typically start with physical models for bond association and dissociation [17]. Combined with the hydrodynamics of a sphere in front of a wall, they

lead to algorithms known as adhesive dynamics [18]. This approach has been applied before to different aspects of rolling adhesion, e.g., the interplay of two receptor systems [19] or the effect of catch bonds [20]. Recently we have developed a different variant of this algorithm which in contrast to earlier approaches fully resolves the spatial positions of the receptors on the sphere and the ligands on the wall. Using this approach, we were able to predict the efficiency of initiating cell adhesion in shear flow as a function of the density and geometry of the receptor and ligand patches [21,22]. A large modeling effort has also been spent on the role of cell deformability [23–27] and the interaction between multiple particles [27–29]. Here we focus on the case of moderate shear flow and small numbers of cells, when cell deformability and hydrodynamic interactions between cells are not relevant [22].

A convenient way to present the results from adhesive dynamics simulations of rolling adhesion is the calculation of state diagrams which predict different types of motion over a large range of model parameters [30,31]. Because in flow chamber experiments one usually measures only translational velocity as a function of time, these state diagrams have been determined before based only on the translational velocity simulated as a function of different molecular parameters. However, computer simulations also allow to track the angular velocity of a cell, thus doubling the number of degrees of freedom that could be compared. For example, in physical terms cell rolling means that translation and rotation are synchronized. Although this fact was already noted in the pioneering paper on adhesive dynamics [18], it has not been systematically exploited due to the lack of experimental data. Here we present a detailed analysis of the different dynamic states of rolling adhesion which is based on the simultaneous tracking of both translational and rotational degrees of freedom. In contrast to earlier work in this field, we fully resolve the spatial positions of receptors and ligands and calculate the state diagrams as a function of the on and off rate. Moreover, we explore the role of different external parameters, including the viscosity of the medium.

The paper is organized as follows. In Sec. II we explain our numerical method, which is a combination of a Langevin equation accounting for hydrodynamic and thermal forces in the limit of small Reynolds numbers (Stokesian dynamics) [32] and adhesive dynamics accounting for the forces caused by the formation of adhesive bonds between cell and substrate [18]. By taking care of the diffusive motion of the sphere, we are able to explicitly resolve both receptor and ligand positions. As a first application of the hydrodynamic part of our model, we explain the physical difference between slipping and rolling. We close this section with a detailed description of the parameters relevant for the algorithm. In Sec. III we point out, using a simple analytical description, how the cell slows down and simultaneously synchronizes its translational and angular velocity under the action of bonds. Then we discuss the mean velocities of the cell as a function of the on and off rate of the receptor-ligand bonds. Based on this we define five distinct states of stationary motion for a cell in a flow chamber. In Sec. IV we identify these different states in state diagrams displaying the dependence on the internal bond parameters, i.e., the on and

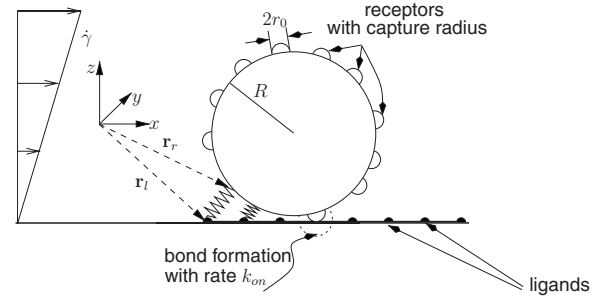


FIG. 1. Model system and adhesive dynamics. A rigid sphere of radius R moves above a wall. The shear flow is linear with shear rate $\dot{\gamma}$. Receptors are modeled as sticky spheres with capture radius $r_0 \ll R$ on the surface of the sphere. Ligands are modeled as dots on the boundary wall. A receptor-ligand bond forms with rate k_{on} whenever a receptor patch has some overlap with a ligand. Bonds are modeled as Hookean springs and exert a force on the sphere that is proportional to the distance between the receptor position \mathbf{r}_r and the ligand position \mathbf{r}_l . They rupture with a force-dependent rate $k_{off}(F)$.

off rate. In addition, the effect of external parameters to the location of the states in the space of different on and off rates is discussed. In the closing section, Sec. V, we argue that molecular parameters can be much better extracted from flow chamber experiments if both translational and rotational degrees of freedom are measured, as it is done in our simulations. Furthermore we propose experiments based on recent nanotechnological developments that could result in flow chamber data for the angular velocities of cells or microspheres.

II. MODEL AND SIMULATION METHOD

A. Stokesian dynamics

As a simple model system for a cell or a microsphere in a flow chamber we use a rigid sphere of radius R that moves above a wall (cf. Fig. 1). For objects as small as white blood cells (with diameters $< 10 \mu\text{m}$) the typical value for the Reynolds number is much less than one and inertia can be neglected (overdamped motion). Therefore, the flow around the cell is laminar and well described by the linear Stokes equation. Cells are usually observed only close to the wall, that is at a distance to the wall which is much smaller than the separation between the two parallel glass plates used in a flow chamber. In this region the unperturbed flow profile is approximately linear. Throughout this paper we therefore consider the sphere to flow in simple shear flow, i.e., we consider the shear rate $\dot{\gamma}$ to be a constant.

In the situation under consideration the sphere is not only driven by the imposed shear flow but also by direct forces exerted on the cell. These include a constant gravitational drift force which results from a slight density difference between the cells and the surrounding medium. For flow chamber experiments, this implies that most cells adhere to the bottom plate, which usually is also the plate coated with ligands. In our context, the strongest forces result after initial binding from receptor-ligand bonds that pull on the sphere. A

third source of force are thermal forces which are ubiquitous for objects in the micrometer range and lead to diffusive motion. This kind of motion can be described by an appropriate Langevin equation. It is convenient to introduce a six-dimensional state vector \mathbf{X} which includes both the three translational and the three rotational degrees of freedom. The first three components of \mathbf{X} denote the Cartesian coordinates with respect to a flow chamber based coordinate system (cf. Fig. 1). The last three components describe the rotation that maps a coordinate system fixed to the center and the orientation of the sphere to the flow chamber fixed coordinate system. Similar compact notations are introduced for velocities and forces. The symbol \mathbf{U} denotes a six-dimensional velocity with the first three components being translational velocities and the last three being angular velocities. \mathbf{F} is the combined force and torque vector. Using this notation, the Langevin equation describing the motion of the cell reads [22]

$$\dot{\mathbf{X}} = \mathbf{U}^\infty + M(\mathbf{F}^S + \mathbf{F}^D) + k_B T \nabla M + \mathbf{g}_t^I. \quad (1)$$

Here, M is the 6×6 mobility matrix. $\mathbf{U}^\infty \propto \dot{\gamma}$ is the velocity of the unperturbed shear flow at the position of the center of the sphere. $\mathbf{F}^S \propto \dot{\gamma}$ is the shear force, which results from the hydrodynamic interaction between the cell and the wall. \mathbf{F}^D denotes all direct forces (torques) acting on the sphere, such as gravity and bond forces. The terms $k_B T \nabla M$ and \mathbf{g}_t^I describe the effect of thermal noise. \mathbf{g}_t^I is Gaussian white noise with

$$\langle \mathbf{g}_t^I \rangle = 0, \quad \langle \mathbf{g}_t^I \mathbf{g}_{t'}^I \rangle = 2k_B T_a M \delta(t - t'). \quad (2)$$

Here T_a is the ambient temperature and k_B Boltzmann's constant. The mobility matrix for a sphere above a wall depends the distance between sphere and wall [33]. Thus, the noise is multiplicative, leading to the gradient term ∇M in Eq. (1). We interpret the noise \mathbf{g}_t in the usual Stratonovich sense. However, Eq. (1) is written in its Itô version [34,35], as indicated by the superscript I . This allows to directly derive a simple Euler algorithm for the update step $\Delta \mathbf{X}$ of the configuration of the sphere during a time step Δt . In nondimensional form, using the radius R of the sphere as the length scale, the inverse shear rate $1/\dot{\gamma}$ as the time scale, and $6\pi\eta R^2 \dot{\gamma}$ as the force scale, the first order discretized version of Eq. (1) reads

$$\begin{aligned} \Delta \mathbf{X}_t = & [\mathbf{U}^\infty + M(\mathbf{F}^S + \mathbf{F})] \Delta t + \frac{1}{\text{Pe}} \nabla M \Delta t + \sqrt{\frac{1}{\text{Pe}}} \mathbf{g}(\Delta t) \\ & + O(\Delta t^2). \end{aligned} \quad (3)$$

Here the dimensionless Péclet number $\text{Pe} = (6\pi\eta R^3 \dot{\gamma}) / (k_B T_a)$ describes the relative importance of convective versus diffusive motion of the sphere. The first two moments for the Gaussian white noise now read

$$\langle \mathbf{g}(\Delta t) \rangle = 0, \quad \langle \mathbf{g}(\Delta t) \mathbf{g}(\Delta t) \rangle = 2M \Delta t. \quad (4)$$

The algorithm, Eq. (3), is also known as Stokesian dynamics and has been derived, e.g., by Brady and Bossis [32] and for vanishing shear flow by Ermak and McCammon [36]. A more detailed description of our algorithm is given in Refs.

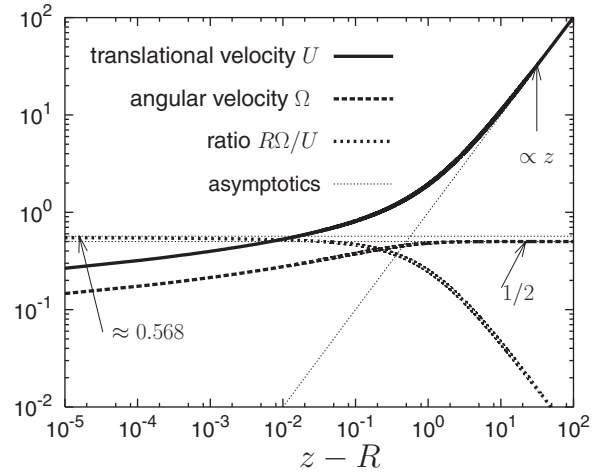


FIG. 2. Velocities of the sphere in the limit of deterministic motion, $\text{Pe} \rightarrow \infty$. Translational and angular velocity U and Ω , respectively, and their ratio $R\Omega/U$ are shown as a function of the separation $z-R$ between sphere and wall. The thin lines depict the asymptotic behavior for $z \rightarrow R$ and $z \rightarrow \infty$, respectively. U and Ω are plotted in units of $R\dot{\gamma}$ and $\dot{\gamma}$, respectively. z is measured in units of R .

[22,37]. In order to obtain accurate results when simulating the motion of the sphere it is essential to properly calculate the mobility matrix M and the shear force \mathbf{F}^S . In our simulations we use a numerical method described by Jones *et al.* [33,38] which allows to accurately calculate the components of the mobility matrix for a single sphere above a wall for arbitrary sphere wall distances. The values obtained by this method agree very well with the classical results given for some tabulated height values by Goldman *et al.* [39].

From Eq. (3) one readily sees that diffusive motion is less relevant if the Péclet number Pe is large. Using typical values for white blood cells (cf. Table I) one finds that Pe is of the order 10^4 . Therefore, regarding the motion in flow direction thermal motion can be neglected on the scale of the cell radius. However, for the motion in z direction the only force on a freely flowing cell is gravitation, which is small due the small density difference between the cell and the surrounding medium and therefore comparable to thermal forces in this direction [22]. For this reason, in our work we use the full Langevin equation from Eq. (1). Another reason why we keep the diffusion terms in Eq. (3) despite the large Pe values has to do with the size of the receptors on the surface of the cell and will become more apparent in the next section, Sec. II B.

For the following it is important to consider how the translational velocity U (in x direction) and the angular velocity Ω (for rotations about the y axis) behave in the limits of small and large separation from the wall. If the translational and angular velocities were completely synchronized, the ratio $R\Omega/U$ should be equal to unity. This would correspond to rolling in a macroscopic sense, e.g., for a sticky sphere rolling down an inclined plane or for a car wheel on the street. We now show that the situation is different for a cell in free hydrodynamic motion. For z denoting the height of the center of the sphere above the wall, $z-R$ denotes the gap between sphere and wall. In Fig. 2 we plot U and Ω as a

function of $z-R$ in the limit of deterministic motion, $Pe \rightarrow \infty$. For the sphere far away from the wall, $z-R \rightarrow \infty$, we have the case of free flow, thus $U = \dot{\gamma}z$ and $\Omega = 1/2$. Therefore the ratio $R\Omega/U$ vanishes in this limit. For the sphere approaching the wall, $z-R \rightarrow 0$, both U and Ω slowly approach zero due to the hydrodynamic no-slip boundary condition. The ratio $R\Omega/U$, however, approaches a finite limit $R\Omega/U \approx 0.5676$ as computed by Goldman *et al.* [39]. Together these results show that hydrodynamic interactions increasingly synchronize translational and angular velocities as the cell approaches the wall. However, the ratio $R\Omega/U$ never reaches the value 1 as it would for rolling in a macroscopic sense. Therefore, the hydrodynamic coupling between the cell and the wall is not strong enough to lead to rolling and a freely moving cell is always slipping.

B. Bond dynamics

We now include receptors, ligands, and receptor-ligand bonds into our model. Throughout this paper we call the cellular part of a bond *receptor* and its counterpart on the wall *ligand*. Before a cell receptor can react with a wall ligand to form a complex (bond), there must be a physical transport process which brings the two components to close proximity. Formally bond formation can be separated into a transport and a reaction step using the notion of an encounter complex [40]. The encounter complex is formed whenever a receptor and a ligand are less than the capture radius r_0 away from each other. Therefore, we model receptors as *reactive patches* on the sphere surface having a spherical capture range of radius r_0 . The capture length r_0 bridges the gap between the continuum approach followed by implementing linear hydrodynamics and the discrete nature of the receptor molecules. Ligands are modeled as dots on the boundary wall. Because we explicitly resolve receptor and ligand positions, it is essential to also include diffusive motion in the algorithm, Eq. (3). Although diffusion plays a minor role for the relative position of the cell, it affects the positions of its surface receptors, which are of much smaller size than the sphere itself.

During the time an encounter complex exists it can react to the final receptor-ligand bond complex with the on-rate k_{on} . Reversely, any bond complex can rupture into the encounter state with the off-rate k_{off} . Experimentally it has been found that the dissociation rate depends on the physical force acting on the bond complex [5,6]. These early experiments agreed nicely with the simplest model for bond dissociation under force, which had been conceived first by Bell [17],

$$k_{off}(F) = k_0 \exp(F/F_d), \quad (5)$$

with k_0 the dissociation rate at zero pulling force, F the force on the bond, and F_d the detachment force scale. The Bell model, Eq. (5), can be rationalized using Kramers theory as being a thermally activated escape over a transition state barrier in the presence of an external force [41–44]. Although recent evidence suggests that the dissociation rate shows a more complicated force dependence at small forces [7,8], Eq. (5) has been demonstrated to properly describe the dissocia-

tion process for selectin bonds in the high force regime [14]. Here we use the Bell model for conceptual and computational simplicity.

In order to include the probabilistic nature of bond formation and rupture, the algorithm, Eq. (3), has to be extended to include rules that take care of these processes. Such rules have been first setup by Hammer and Apte [18] and been refined many times to model various aspects of leukocyte rolling. They are now known as *adhesive dynamics*. Here, we briefly explain the main idea behind these rules. A detailed description of our implementation of these rules is then given in the Appendix. In order to simulate the motion of a cell under the action of bonds, the configuration of the sphere is updated at each time step Δt according to Eq. (3). If, after some update, a receptor patch on the surface of the sphere overlaps with a wall ligand a receptor-ligand bond forms with rate k_{on} , i.e., the probability for bond formation during time step Δt is $1 - \exp(-k_{on}\Delta t)$. Existing bonds are modeled as harmonic springs, i.e., the force along these bonds is proportional to the bond extension, essentially given by $\|\mathbf{r}_r - \mathbf{r}_l\|$, with \mathbf{r}_r and \mathbf{r}_l being the receptor and ligand position, respectively (see Fig. 1). Force and torque resulting from extended bonds then enter the configuration update equation, Eq. (3), via the direct force term \mathbf{F}^D . Similarly to bond formation, the probability for bond rupture during time step Δt is given by $1 - \exp(-k_{off}\Delta t)$, where k_{off} is the force dependent dissociation rate according to Eq. (5).

In contrast to earlier implementations of adhesive dynamics, we explicitly resolve both receptors and ligands in space, rather than considering a wall homogeneously coated with ligands at constant density. One immediate advantage of our method is that it avoids a flow rate-dependent rate of bond formation [45]. In order to be able to spatially resolve both ligands and receptors, it is necessary to include the Brownian motion of the cell. If one considered only the deterministic part of Eq. (1), at low densities of receptors and ligands it could happen that a receptor never finds a ligand. Although these extensions of adhesive dynamics lead to increased computational effort, they are closer to real biological systems, which on the molecular level are in permanent thermal motion. In particular, in the future our implementation will allow us to model receptor-ligand kinetics in more molecular detail. As will be discussed later, our algorithm also opens up the perspective to compare adhesive dynamics simulations to flow chamber experiments using substrates with nanopatterned ligand.

C. Parameters

Our model contains 13 different dimensional parameters. With R , $1/\dot{\gamma}$, $6\pi\eta R^2\dot{\gamma}$ being the natural scales of length, time, and force, respectively, we are left with ten numerical (dimensionless) parameters appearing in the algorithm. Typical values for these (both the dimensional and dimensionless) parameters are listed in Table I. The parameters R , T_a , $\dot{\gamma}$, η , $\Delta\rho$ influence the flow properties and besides viscosity we keep these parameters fixed. For the ambient temperature T_a we choose room temperature $T_a = 293$ K. For flow chamber experiments with cells, the choice $T_a = 310$ K would be

TABLE I. Parameters used for the adhesive dynamics simulations. If no extra symbol for the dimensionless quantity is defined we use the same symbol for both the dimensional and dimensionless representation of this quantity.

Parameter \rightarrow nondimensionalized	Typical value (dimensionless)	Meaning	Reference
$R \rightarrow 1$	$4.5 \dots 5 \mu\text{m}$	radius	[6,46]
$\dot{\gamma} \rightarrow 1$	$50 \dots 150 \text{ Hz}$	shear rate	[14]
T_a	$293 \dots 310 \text{ K}$	ambient temperature	
η	$1 \dots 3 \text{ Pa s}$	viscosity	[14]
$\Delta\rho$	50 kg/m^3	density difference	[47]
κ	$10^{-5} \dots 10^{-2} \text{ N/m}$	bond spring constant	[18,48,49]
$\rightarrow \kappa/6\pi\eta R\dot{\gamma}$	$(10^{-1} \dots 10^3)$		
k_{on}	$10^3 \dots 10^4 \text{ Hz}$	on rate	[10]
$\rightarrow \pi = k_{on}/\dot{\gamma}$	$(10^{-3} \dots 10)$		
k_0	$0.5 \dots 300 \text{ Hz}$	unstressed off rate	[6,50]
$\rightarrow \epsilon_0 = k_0/\dot{\gamma}$	$(10^{-4} \dots 10^3)$		
r_0	50 nm	capture radius	
$\rightarrow r_0/R$	(10^{-2})		
d	$0.1 \dots 1 \mu\text{m}$	ligand-ligand distance	[5,6]
$\rightarrow d/R$	$(0.02 \dots 0.2)$		
x_c	$2 \dots 4 \times 10^{-11} \text{ m}$	reactive compliance	[6]
$\rightarrow 6\pi\eta R^2\dot{\gamma}x_c/k_B T_a$	$(0.1 \dots 0.6)$		
N_r	$50 \dots 5000$	Number of receptors	[18,51,52]
h_{min}	15 nm	minimum cell height	[53]
$\rightarrow h_{min}/R$	(3×10^{-3})		

more appropriate, but the exact choice of this value, which affects bond dissociation kinetics and effective strength of diffusion, turns out to be irrelevant for the physiologically relevant parameter values chosen here. For the Stokes radius R of the cells we use $R=4.5 \mu\text{m}$, which is about the measured radius of neutrophils, a main type of leukocytes undergoing rolling adhesion [46]. The N_r receptor patches are randomly distributed on the cell surface. The receptor patches might be identified with cell microvilli, which are membrane projections to whose tips the selectin receptors are localized [54]. The number of microvilli on a leukocyte varies from several hundreds [52] up to 10 000 [18,51]. In our simulations, we use N_r in the order of 10^3 . Although usually several receptors can be found on the microvilli tips, we allow only one bond per receptor patch, i.e., N_r is also the total number of receptors. Receptors and ligands are spatially extended in the nm range and their binding sites diffuse within some region around their linkage. The diffusion constant of a nm-sized object is about three orders of magnitude larger than that of the cell itself. Therefore, it is sufficient to account for the spatial distribution of the location of binding by introducing a capture sphere with capture radius $r_0=50 \text{ nm}$, which is about the combined length of ligand and receptor [53,55]. In regard to the ligands, we consider them being distributed on a square lattice with lattice constant d . Here, d is obtained from $d=\sqrt{1/N_l}$, with N_l being the average number of ligands per μm^2 . In flow chamber experiments N_l typically varies between $(1-100)/\mu\text{m}^2$ [5,6].

The on-rate k_{on} for single bond formation from a receptor-ligand encounter in Table I is given in units of Hz. Experi-

mentally, it is very difficult to determine this rate directly. Using three-dimensional affinity data, an upper limit has been estimated to be 10^4 Hz [10]. For the force dependent off-rate k_{off} we have the two Bell parameters k_0, F_d , where the detachment force is $F_d=k_B T_a/x_c$ with reactive compliance x_c . Both, unstressed off-rate k_0 and reactive compliance x_c have been measured for different selectin bonds [5,6]. The reactive compliance for L -selectin bonds is $x_c=2 \times 10^{-11} \text{ m}$ [6]. This corresponds to a typical detachment force of 200 pN .

For closed bonds we use the linear force extension curve explained in Sec. II B with spring constant κ . For the P -selectin-PSGL-1 complex Fritz *et al.* [48] measured a value of $\kappa_{RL}=5.3 \times 10^{-3} \text{ N/m}$. Recently, also the role of microvilli elasticity was discussed [31]. Shao *et al.* determined the spring constant of microvilli in the low force regime to be $\kappa_{mv}=4.3 \times 10^{-5} \text{ N/m}$ [49]. The total spring constant $\kappa = \kappa_{mv}\kappa_{RL}/(\kappa_{mv} + \kappa_{RL})$ of the microvilli and bond series would then be dominated by the microvilli spring constant. Besides the bond forces, we include only the buoyant force due to the small density difference $\Delta\rho$ between the cell and the surrounding medium. Other nonspecific repulsion forces arising from electrostatic and steric stabilization forces are effectively taken into account by introducing a simulation rule that the cell can approach the wall only up to a distance of $h_{min}=15 \text{ nm}$ [53]. In a physiological system, this would correspond to the thickness of the glycocalyx, a protective layer of sugar covering the endothelium in blood vessels.

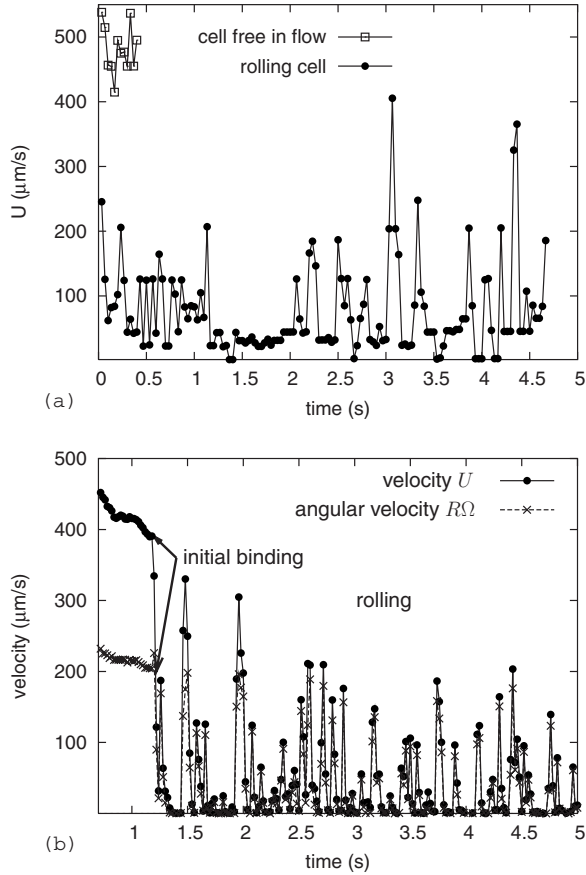


FIG. 3. Snapshots of leukocyte motion. (a) Velocity of a leukocyte (neutrophil) rolling on *L*-selectin ligand peripheral node addressin (PNAd) with 60 sites per μm^2 . [Data obtained from Ref. [6], Fig. 1(a)] (b) Translational and angular velocity (U and $R\Omega$, respectively) of a sphere with radius $R=5 \mu\text{m}$ measured in adhesive dynamics simulation at the same ligand density (with on rate $k_{on}=60 \text{ Hz}$ and unstressed off rate $k_0=6.8 \text{ Hz}$).

III. DEFINITION OF THE DYNAMIC STATES OF MOTION

A. Experiment and simulation

Having completed the model definition, we now start to analyze the simulation results. For the following we first have to clarify what is meant by the velocity of the cell. As we include Brownian motion, the velocity of the cell $U(t)$ cannot be its instantaneous velocity, because for the trajectory of a Brownian particle $\lim_{\delta t \rightarrow 0} [X(t+\delta t) - X(t)] / \delta t$ is not a well-defined quantity [56]. Thus, we define the velocity of the sphere at time t by a difference quotient $U(t) := [X(t+\Delta t) - X(t)] / \Delta t$ with some time interval Δt . Throughout this paper, we choose $\Delta t = 0.02 \text{ s}$, which corresponds to a camera resolution of 50 Hz. The angular velocity for rotations about the y -axis $\Omega(t)$ is defined in a similar way.

In Fig. 3 we compare in a qualitative way the data obtained in a numerical simulation of leukocyte motion with data of a rolling cell obtained in a flow chamber experiment. In Fig. 3(a) the translational velocity U (denoting the velocity in the direction of imposed shear flow) of a rolling leukocyte for some period of time is shown as experimentally

measured by Alon *et al.* [6]. The rolling state is identified by a strong decrease of the average cell velocity compared to the average velocity of a cell moving freely in hydrodynamic flow. Figure 3(b) shows a representative trajectory from our simulations. No attempt has been made to fit this data set to the experimental one. Yet it is clear that both data sets show very similar features, including the strong decrease of velocity upon binding and the subsequent bursts in velocity, which correspond to stochastic rupture events at the trailing edge allowing for cell movement. In contrast to the experimental data, the simulation data also records the angular velocity $R\Omega$. The simulation reveals that the $R\Omega$ and U curves collapse onto one curve as soon as the cell binds for the first time (at $t \approx 1.2 \text{ s}$). Before initial binding, the cell slips over the substrate with $R\Omega/U < 0.57$ as discussed in Sec. II A. This observation motivates us to define the dynamic state of *rolling* by $R\Omega/U \rightarrow 1$, in accordance with the common understanding of this term in macroscopic mechanics. However, before we develop this idea in more detail in Sec. III C, we first show with an analytical calculation how the action of a bond synchronizes translational and rotational velocities.

B. Stopping-process: Emergence of rolling

In order to understand how the cell comes to a stop after the first bond has been formed, in the following we consider a set of simplified equations of motion. We reduce our analysis to a two-dimensional case in which the cell is only allowed to translate in the x direction and to rotate about the y axis. These 2 degrees of freedom are called x for the translational and θ for the rotational degree of freedom, respectively. In regard to the z direction we assume that the cell moves at constant height above the wall ($\dot{z}=0$) with $z=R+r_0$. Furthermore, we neglect Brownian motion, i.e., we consider the limit $\text{Pe} \rightarrow \infty$. Then, the equations of motion for the two coordinates read (with $\dot{x}=U$ and $\dot{\theta}=\Omega$, cf. Sec. II A)

$$\begin{pmatrix} \dot{x} \\ \dot{\theta} \end{pmatrix} = M_{x\theta} \begin{pmatrix} F_{B,x} \\ T_{B,y} \end{pmatrix} + \begin{pmatrix} U_{hd} \\ \Omega_{hd} \end{pmatrix}, \quad (6)$$

with $F_{B,x}$ the x component of the bond force and $T_{B,y}$ the y component of the torque which is due to the bond (see Fig. 4). Because the bond is modeled as a linear spring, it has mechanical properties and we call it a *tether*. The matrix $M_{x\theta}$ denotes the $(x\theta)$ sector of the mobility matrix introduced in Eq. (1). If no bond is formed, then $F_{B,x}=T_{B,y}=0$, and $U=U_{hd}$ and $\Omega=\Omega_{hd}$. The free velocity U_{hd} is often referred to as the *hydrodynamic velocity* of the cell. From Fig. 4 we read off tether force and tether torque \mathbf{F}_B and \mathbf{T}_B , respectively:

$$\mathbf{F}_B(t) = \kappa \begin{pmatrix} -x(t) + R \sin(\theta(t)) \\ 0 \\ R \cos(\theta(t)) - z \end{pmatrix}, \quad \mathbf{T}_B(t) = \hat{\mathbf{r}} \times \mathbf{F}_B, \quad (7)$$

$$\hat{\mathbf{r}} = \begin{pmatrix} -R \sin(\theta(t)) \\ 0 \\ -R \cos(\theta(t)) \end{pmatrix}.$$

In the following we distinguish two different cases with respect to the resting length of the bonds. We start with the

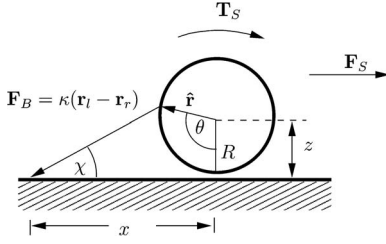


FIG. 4. A cell is stopped by a tether force \mathbf{F}_B . \mathbf{r}_l and \mathbf{r}_r are ligand and receptors position, respectively. x , θ define 2 degrees of freedom, χ the angle between the bond and the wall. In equilibrium (i.e., $U = \dot{x} = 0$, $\Omega = \dot{\theta} = 0$) the shear force \mathbf{F}_S and the shear torque \mathbf{T}_S are balanced by the tether force and its respective torque. Not shown are gravitational force and repulsive forces from the substrate that compensate all downward acting forces.

case where we assume the resting length to be zero. With the cell moving at a constant height $z = R + r_0$, at $t = 0$ already a small bond force in z direction exists (but no torque). Briefly after bond formation the cell has not moved significantly and $x/R, \theta \ll 1$ holds. Thus, the quantities $F_{B,x}, T_{B,y}$ can be approximated as

$$F_{B,x} = \kappa(R\theta - x) + O(\theta^3),$$

$$T_{B,y} = \kappa(Rx - zR\theta) + O(\theta^3) + O(x\theta^2). \quad (8)$$

Reinserting these approximate expressions into Eq. (6), we obtain a first order linear differential equation for x, θ

$$\begin{pmatrix} \dot{x} \\ \dot{\theta} \end{pmatrix} = C \begin{pmatrix} x \\ \theta \end{pmatrix} + \begin{pmatrix} U_{hd} \\ \Omega_{hd} \end{pmatrix}, \quad C := M_{x\theta}^{-1} X, \quad X := \kappa \begin{pmatrix} -1 & R \\ R & -zR \end{pmatrix}, \quad (9)$$

which can readily be solved with the proper boundary conditions [$x(0) = \theta(0) = 0$]. The determinant of the matrix C is $\det C = \kappa^2 R(z-R) \det M_{x\theta}$. From the dissipative nature of the mobility matrix expressed, e.g., in Eq. (2), it follows that $M_{x\theta}$ is positive definite, which is then also true for the matrix C . As the diagonal elements of $M_{x\theta}$ are significantly larger than the off-diagonal element [38,33], one easily finds that $\text{tr} C$ is negative. Therefore, C has two negative eigenvalues, which we denote in the following by λ_{\pm} . As $z-R \ll R$ one can approximate $\lambda_+ \approx \text{tr} C$ and $\lambda_- \approx \det C / \text{tr} C$. These two eigenvalues represent two different timescales with $|\lambda_-| \ll |\lambda_+|$. With this the solution to Eq. (9) can be written as

$$\begin{pmatrix} x(t) \\ \theta(t) \end{pmatrix} = \begin{pmatrix} 1 \\ \frac{\lambda_+ - (C)_{11}}{(C)_{12}} \end{pmatrix} \frac{U_{hd} + \lambda_- x_{\infty}}{\lambda_- - \lambda_+} (1 - e^{\lambda_+ t}) - \begin{pmatrix} 1 \\ \frac{\lambda_- - (C)_{11}}{(C)_{12}} \end{pmatrix} \frac{U_{hd} + \lambda_+ x_{\infty}}{\lambda_- - \lambda_+} (1 - e^{\lambda_- t}), \quad (10)$$

where the asymptotic solution after the cell has stopped is given by

$$\begin{pmatrix} x_{\infty} \\ \theta_{\infty} \end{pmatrix} := - (C)^{-1} \begin{pmatrix} U_{hd} \\ \Omega_{hd} \end{pmatrix}. \quad (11)$$

Equation (11) is the linearized version of the force and torque balance condition at mechanical equilibrium. In non-linearized form the force and torque balance equation reads

$$\begin{pmatrix} F_{B,x} \\ T_{B,y} \end{pmatrix} = - M_{x\theta}^{-1} \begin{pmatrix} U_{hd} \\ \Omega_{hd} \end{pmatrix}.$$

Then, for $z = 1.01R$ one obtains $F_{B,x} \approx -1.7 \times 6\pi\eta\gamma R^2$ and $T_{B,y} \approx -0.6 \times 6\pi\eta\gamma R^3$ [39]. The relation to the quantities x_{∞}, χ is given in Ref. [6],

$$\|\mathbf{F}_B\| \cos \chi = \|\mathbf{F}_S\|, \quad \|\mathbf{F}_B\| x_{\infty} \sin \chi = \|\mathbf{T}_S\| + R \|\mathbf{F}_S\|. \quad (12)$$

The relation with θ_{∞} is given by the purely geometrical relation $x_{\infty}/R = \sin \theta_{\infty} + (1 - \cos \theta_{\infty})/\tan \chi$ (cf. Fig. 4). In contrast to the linear version, Eq. (12) cannot be solved for $x_{\infty}, \theta_{\infty}$.

The initial velocities of the cell are the free hydrodynamic velocities with $R\dot{\theta}(0)/\dot{x}(0) \approx 0.5$ so that x and θ do not increase at the same speed [see Fig. 5(a)]. Shortly after bond formation, $t \ll 1/|\lambda_+|$, $\exp(\lambda_+ t) \approx 0$ and the time development of x, θ is governed by the second term in Eq. (10). At intermediate times t_{int} with $1/|\lambda_+| \ll t_{int} \ll 1/|\lambda_-|$ the velocities are approximately given by

$$\begin{pmatrix} \dot{x} \\ \dot{\theta} \end{pmatrix} \approx \lambda_- \begin{pmatrix} 1 \\ \frac{\lambda_- - (C)_{11}}{(C)_{12}} \end{pmatrix} \frac{U_{hd} + \lambda_+ x_{\infty}}{\lambda_- - \lambda_+} e^{\lambda_- t_{int}}. \quad (13)$$

Expanding $R\dot{\theta}/\dot{x}$ in powers of $(z-R)/R \ll 1$, we obtain $R\dot{\theta}/\dot{x} = 1 + O((z-R)/R)$ which reflects the definition of rolling in mechanics. Thus, by the action of force and torque resulting from the tether bond, translational and angular velocity of the cell are adjusted and the cell starts rolling a short time after the first bond is formed. This can be seen in Fig. 5(a), there the two velocities $\dot{x}, \dot{\theta}$ are plotted as a function of time. Although Eq. (10) correctly predicts the cell to arrest at large times, the linear approximation Eq. (8) is not applicable at these times, as can be seen from Fig. 5. In Fig. 5(a) the cell velocities as predicted from the analytical solution to Eq. (9) are compared to the velocities which are obtained when Eq. (6) is numerically integrated. We see that for short times the linear approximation works quite well, until the cell has reached its rolling state (i.e., $R\Omega/U \approx 1$). At long time scales the approximate solution provides only a qualitative prediction of the stopping process. The figure shows that the higher order terms contributing to the bond force and/or torque lead to a much faster stopping than predicted by the approximation of these quantities with respect to first order in x, θ [see Eq. (8)].

We now briefly discuss the case of a nonvanishing resting length l_0 of the bond (a nonvanishing resting length with $l_0 \ll r_0$ is used in our simulations as explained in the Appendix). For this we assume the height $z-R$ of the cell above the wall to be equal to the resting length of the tether bond. In that case the spring constant in Eq. (7) is replaced by $\kappa \rightarrow \kappa(1 - l_0/|\mathbf{r}_l - \mathbf{r}_r|)$ (see Fig. 4). The leading order term in the power series of $F_{B,x}$ is then of second order in x, θ . Thus

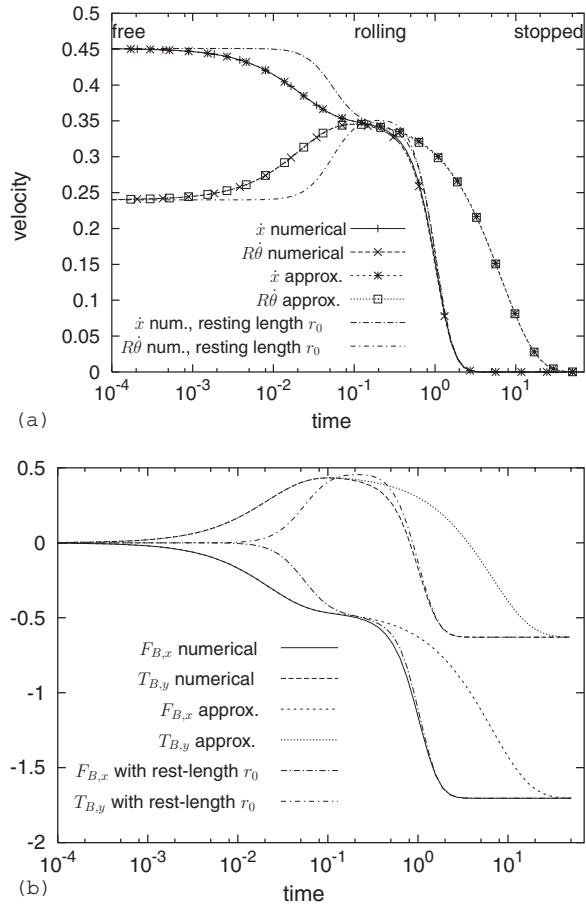


FIG. 5. Comparison of the analytical solution for the stop dynamics mediated by a single bond Eq. (10) with values obtained from numerical integration of Eq. (6) ($z=1.01R$). All plotted quantities are in dimensionless form, i.e., force is expressed in terms of $6\pi\eta R^2\dot{\gamma}$, torque in terms of $6\pi\eta R^3\dot{\gamma}$, velocity in $\dot{\gamma}R$, and time in $1/\dot{\gamma}$. For the dimensionless spring constant $\kappa=10^2$ was used. For a set of typical parameter values: $R=5\ \mu\text{m}$, $\dot{\gamma}=100\ \text{Hz}$, $\eta=10^{-3}\ \text{Pa s}$, $\kappa=1$ corresponds to $10^{-5}\ \text{N/m}$. (a) Plot of the (angular) velocity \dot{x} ($\dot{\theta}$) as a function of time for three different calculations: from numerical integration of Eq. (6), from analytical derivative of Eq. (10), and from numerical integration of Eq. (6) under the assumption that the initial bond length r_0 is the resting length of the bond $l_0=r_0$. For the time axis a logarithmic scale is used. (b) The same for the bond force (torque) $F_{B,x}$ ($T_{B,y}$).

the linear approximation of the equations of motion cannot be applied in this case and therefore we consider this case only numerically. The results are also shown in Fig. 5(a). We note that the qualitative behavior is very similar to the case of zero bond resting length. Figure 5(a) shows that at short times the cell moves on with almost unchanged velocities, then the velocities adjust to $R\dot{\theta}\approx\dot{x}$ (for some time even $R\dot{\theta}>\dot{x}$) and finally the cell stops after about the same time as in the case with zero bond resting length.

The linearized analysis of the rather complex motion of the cell under the action of a single bond might appear to be somehow simplifying, but it nicely reveals the mechanism that leads to cell rolling. This can best be understood from the time dependence of the torque that is exerted by the

tether, see Fig. 5(b). In our approximation the torque is given by $T_{B,y}=\kappa(Rx-zR\theta)$ [see Eq. (8)]. Initially, x increases faster than $R\theta$ and as $z\approx R$ the torque is positive, i.e., it supports the shear torque and the cell starts turning faster. At the same time the force $RF_{B,x}\approx-T_{B,y}$ slows down the translational motion. The maximum torque $\dot{T}_{B,y}=0$ is reached when $z\dot{\theta}=\dot{x}$, i.e., when the cell is approximately rolling. From that time on x and θ increase at approximately the same speed and eventually the torque will become negative (if $x<z\theta$) and will act against the shear torque. Similar arguments hold when repeating the previous discussion with the exact expression for the torque given in Eq. (7).

C. Cell motion at multiple bonds: Classification of states of motion

The previous analysis did only include a single bond which in addition was not allowed to rupture. In the presence of multiple bonds permanently forming and rupturing the situation is much more complex. Whether a cell is able to roll or not depends then on the one hand on *external* parameters such as ligand density, shear rate, and viscosity. On the other hand it depends also on the *internal* parameters of the single receptor-ligand complex, which in our model are the on rate k_{on} , the off rate k_0 , and the detachment force F_d . In the following we will present our results mainly as a function of the two internal rates in their dimensionless form, $\pi=k_{on}/\dot{\gamma}$ and $\epsilon_0=k_0/\dot{\gamma}$. In Fig. 6(a) we plot the mean translational and angular velocities as well as the standard deviation of the translational velocity, $\sigma_U=\sqrt{\langle U^2\rangle-\langle U\rangle^2}$ (where the average is an average over time and an ensemble of cells), in a large range of values for the dimensionless on and off rates. To further illustrate the dependence of the kinetic quantities on the on and off rate, in Fig. 6(b) the ϵ_0 dependence at fixed on rate π is replotted. At $\pi=10$, one sees that with decreasing ϵ_0 , translational and angular velocities first approximate each other, i.e., U decreases and $R\Omega$ increases. Then, both together decrease to zero at very low off rates. At smaller on rates ($\pi=0.04$), both U and $R\Omega$ monotonically decrease with decreasing off rate and $R\Omega\approx U$ occurs only when both quantities are close to zero. The standard deviations of the velocities $\sigma_U, \sigma_{R\Omega}$ are small for very low and very high off rates. In between, they pass through a maximum which is located exactly at the transition from unperturbed motion to cell arrest ($U\approx R\Omega\approx 0$). We now summarize these qualitative observations by defining five different classes of stationary states of cell motion (see also Table II).

Free motion. We call a cell to move freely if its speed is larger than $0.95U_{hd}$ [an example is shown in Fig. 7(a)]. Free motion as we define it does not imply that there are no bonds at all. The definition given by us rather allows also for bonds with a very fast dissociation rate (off rate) or very small detachment forces. In this case existing bonds dissociate before they are stretched enough to apply forces that slow down the mean velocity of the cell below 95% of U_{hd} .

Firm adhesion (arrest). This is the state when the mean translational velocity $\langle U\rangle$ is less than $0.01U_{hd}$ [Fig. 7(b)]. This still allows for small jumps due to rare dissociation events. Besides that tether bonds compensate shear force and torque (cf. Sec. III B).

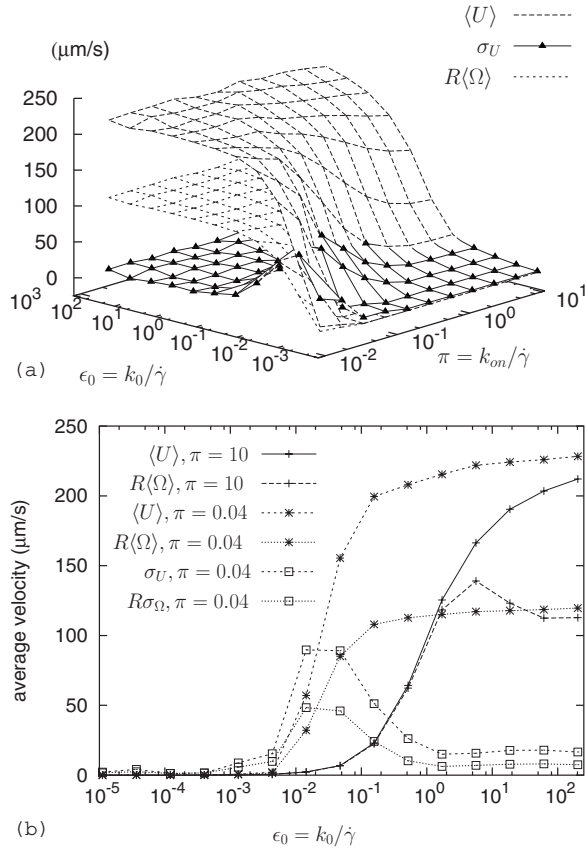


FIG. 6. (a) Mean velocity $\langle U \rangle$, its standard deviation σ_U , and mean angular velocity $R\langle \Omega \rangle$ as functions of the dimensionless rates π , ϵ_0 . (b) $\langle U \rangle$, $R\langle \Omega \rangle$, σ_U , $R\sigma_\Omega$ as functions of the unstressed off-rate ϵ_0 for two different on-rates π . Parameters used for these simulations: $R=4.5 \times 10^{-6}$ m, $T=293$ K, $\dot{\gamma}=100$ Hz, $\Delta\rho=0.05 \times 10^3$ kg/m³, $\eta=1.002 \times 10^{-3}$ Pa s, $\kappa=1 \times 10^{-3}$ N/m, $r_0=1.0 \times 10^{-2}R$, $d=5 \times 10^{-2}R$, $N_r=5000$, $x_c=2 \times 10^{-11}$ m. The average was obtained over ten simulation runs of 20 s duration.

Rolling adhesion. The ratio $R\langle \Omega \rangle / \langle U \rangle$ is larger than 0.8. As was shown in Sec. II A, this is well above the hydrodynamic maximum of this ratio in the limit $z \rightarrow R$ (i.e., when the cell touches the wall). Figures 7(e) and 7(f) show two examples of computational leukocyte rolling.

Transient adhesion. If none of these criteria applies we define the state as being transient. Within this category we distinguish two subclasses according to the standard deviation σ_U . By $\sigma_U / \langle U \rangle < 0.5$ the first subclass (*transient I*) is defined, otherwise the cell's motion is in the subclass *transient II*. “Transient I” occurs if bonds form and rupture per-

manently, so that they reduce the (translational) velocity considerably below the hydrodynamic velocity. However, in this case the bonds do not last sufficiently long as to increase the ratio $R\langle \Omega \rangle / U$ above 0.8. Figure 7(c) shows an example for this kind of motion. “Transient II” is characterized by alternating periods of arrest and free motion which is illustrated in Fig. 7(d).

As the kinetic quantities $\langle U \rangle$, $\langle \Omega \rangle$, σ_U vary continuously with respect to π and ϵ_0 , the classification given above is not unique. But it allows to clearly distinguish these states in an *on-off state diagram*, i.e., the states are in general not degenerated. Other classifications of leukocyte states have been given before. For example, in the first paper on adhesive dynamics also five states of motion were defined [18]. In contrast to our definition, however, this classification was only qualitative. In computer simulations of adhesive dynamics or other numerical models for rolling adhesion, it is common to define states of motion such as *free*, *rolling*, and *firm adhesion*, but usually this is done in an experimental context, which means that these classifications are based only on the mean translational velocity [31,57]. A classification into *immobile*, *rolling*, and *detached* and a corresponding state diagram has also been given by Bruinsma in a mean field approach, which did not model in detail how force is distributed over the molecular bonds [58].

IV. STATE DIAGRAM OF LEUKOCYTE MOTION

In order to determine the stationary state of motion for a given set of parameters, we repeatedly performed the following computer simulation. At a given set of parameter values we let the cell start at a height $z=R+r_0$ and subsequently simulate its motion for 20 s. As a result of the downward acting buoyant force, which drives the cell even closer to the wall, the wall ligands will be immediately within the capture range of the cell receptors. Then, as shown in [21], the mean time for receptor-ligand encounter is close to zero for typical ligand and receptor densities found for leukocytes. Therefore, cell-wall interactions arising from bonds are assumed to influence the cell motion for the complete run of the simulation. To nevertheless rule out any initialization effects the mean values and variances for U, Ω are only calculated for times greater than 4 s, i.e., 20% of the total run length of 20 s. To ensure proper classification of the state of motion, each simulation run is repeated at least ten times (each time with another randomly chosen receptor distribution) and each run contributes to the mean values $\langle U \rangle$, $\langle \Omega \rangle$ and their standard deviations σ_U, σ_Ω (in the case that σ_U is large even

TABLE II. Five stationary states of leukocyte motion.

State	Definition
Free motion	$\langle U \rangle > 0.95 U_{hd}$
Rolling adhesion	$R\langle \Omega \rangle / \langle U \rangle > 0.8$ and $0.95 > \langle U \rangle / U_{hd} > 0.01$
Firm adhesion	$\langle U \rangle < 0.01 U_{hd}$
Transient adhesion I	$0.01 < \langle U \rangle / U_{hd}$ and $R\langle \Omega \rangle / \langle U \rangle < 0.8$ and $\sigma_U / \langle U \rangle < 0.5$
Transient adhesion II	$0.01 < \langle U \rangle / U_{hd}$ and $R\langle \Omega \rangle / \langle U \rangle < 0.8$ and $\sigma_U / \langle U \rangle > 0.5$

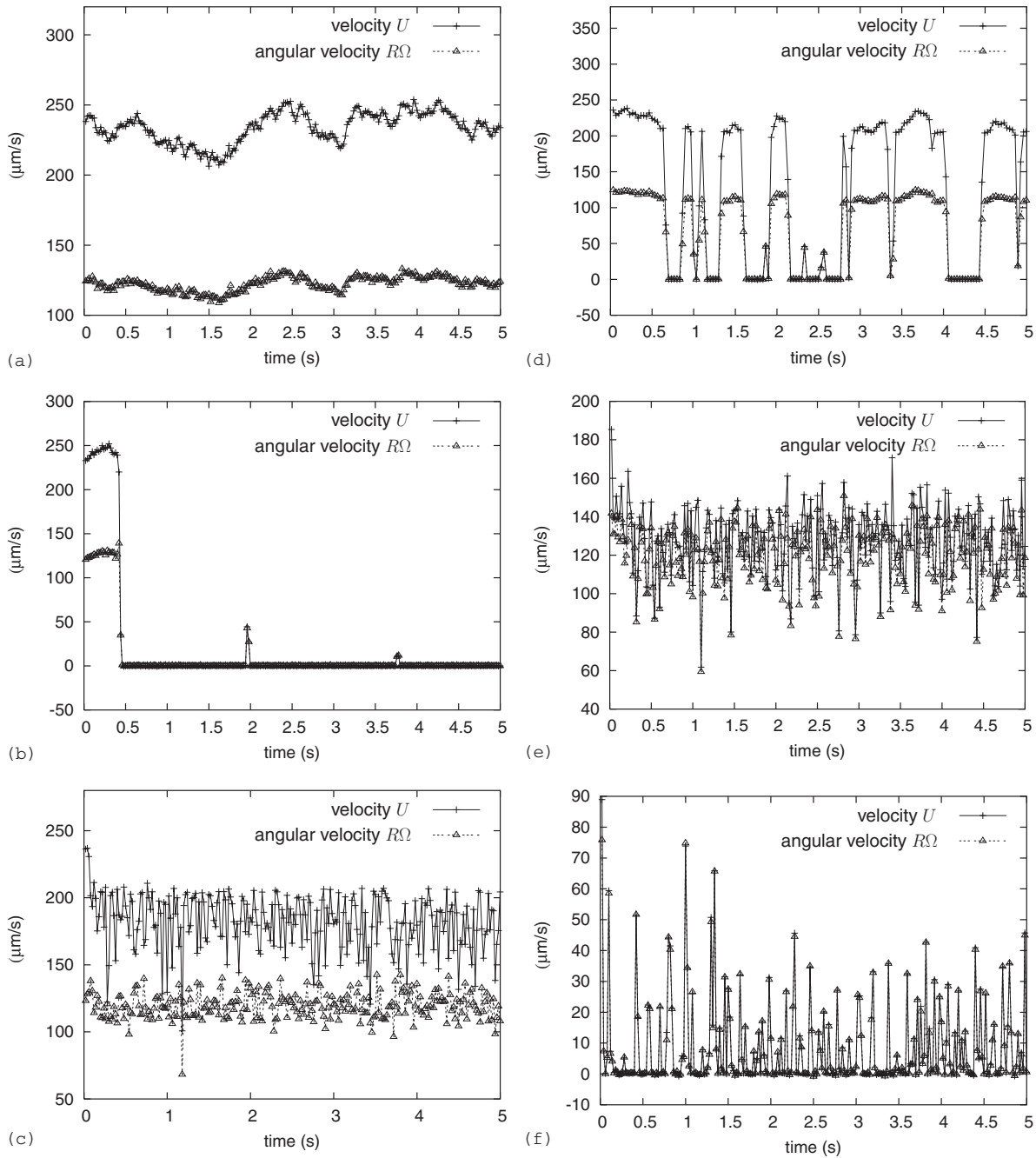


FIG. 7. (a) Translational and angular velocities U and $R\Omega$, respectively, that give examples of the different states of leukocyte motion defined in this section. The labels (a)–(f) refer to the numbered points in the state diagram shown in Fig. 8. (a) Free motion, (b) firm adhesion, (c) “transient I,” (d) “transient II,” (e), (f) rolling adhesion.

more than ten simulation runs were performed). The numerical time step was chosen to be between 10^{-5} – 5×10^{-4} (at a typical shear rate of $\dot{\gamma}=100$ Hz, the lower limit of the numerical time step correspond to real time step of 10^{-7} s). The smaller range of time steps is chosen when high ligand densities or stiff bonds (large κ) are considered [to avoid too large update steps at large direct forces in Eq. (3)]. Keeping the other parameters fixed and varying the rates π, ϵ_0 on a grid in double logarithmic scale, we can determine the different types of leukocyte motion in an *on-off state diagram*.

Figure 8 shows a first example of such a state diagram. The parameters used there are listed in the figure caption of

Fig. 6 (as we keep the parameters $R, T_a, \Delta\rho, r_0$ fixed for all the diagrams shown in this section, they are not explicitly listed for the following state diagrams).

All five states can be identified in Fig. 8 and in Figs. 7(a)–7(f) example trajectories for each of these states are shown. In the limit of very large off-rates ϵ_0 the cell moves freely, i.e., no matter how frequently bonds are formed, force cannot build up because dissociation occurs immediately. At very small off rates the cell is in the state of firm adhesion, i.e., once a bond is formed it lasts long enough to stop the cell and to allow further bonds to be formed, thus stabilizing the cell in its rest position. In between these two limiting

cases for the off rate we find the other three states. From these the rolling state appears only for on-rates π above a certain threshold. This confirms the conclusion drawn from early experiments with flow chambers that selectins are especially suited for rolling adhesion due to their fast on and off rates [6]. The state “transient I” appears when the off rate is too large to support rolling, but still too small to allow for free motion. When both on and off rates are small, the cell is in state “transient II.” In this state the cell stops most likely whenever a bond is formed due to the small off rate. This results in periods of firm adhesion. The small on rate, however, makes it rather unlikely that bonds are formed, which results in periods of free motion. Thus, the cell moves in a stick-slip-like fashion.

The dynamic state diagram Fig. 8 emphasizes that the molecular rates (the on rate π and the off rate ϵ_0) are the main determinants of rolling adhesion. In addition, the state diagram also depends on the other parameters contained in the adhesive dynamics algorithm. In the following we discuss the qualitative dependence on some of these parameters.

A. Medium viscosity

The impact of viscosity is illustrated in Fig. 9(a). There, the on-off diagrams for the fluid viscosities $\eta = 1, 3, 5$ mPa s are shown. The viscosity of the standard medium in which leukocytes are usually perfused through flow chambers is about 1 mPa s. For $\eta = 3$ mPa s the states of motion are distinguished by areas filled with different gray scales. For $\eta = 1, 5$ mPa s only the border lines between two states are shown. The figure legend explains which state can be found below a given line. For the sake of clarity, the original (12,13)-simulation grids for the three diagrams are omitted. Figure 9(a) clearly shows that the main effect of increasing the viscosity is the increase in the range where rolling is possible. More precisely, the larger the viscosity, the lower the off rate ϵ_0 at which firm adhesion sets in. This effect results from the Bell model for bond dissociation. The shear stress $\eta\dot{\gamma}$ and the maximum force in a tether bond are proportional to the viscosity η (the maximum force is the force which holds the cell at rest, see Fig. 4). Therefore, an increase in viscosity from η^* to η increases the off rate similar to

$$\epsilon = \epsilon_0 [\exp(F_B^*/F_d)]^{(\eta/\eta^*)},$$

with F_B^* the bond force at viscosity η^* . As a rough estimate for the bond force we use $F_B^* \approx \|\mathbf{F}_S\|/\cos\chi$ (see Fig. 4 for the definition of \mathbf{F}_S, χ ; for the angle we estimate $\chi \approx 65^\circ$ [6]). Then, for the parameter values used here we have $F_B^*/F_d \approx 0.7$ at $\eta^* = 1$ mPa s. Thus, if at some viscosity η firm adhesion occurs for off rates smaller than a certain value ϵ_0^{firm} , i.e., for $\epsilon_0 < \epsilon_0^{firm}$, then, we expect firm adhesion for η^* to exist at the same rate ϵ . For η^* this rate is estimated to be $\epsilon_0^{firm} \exp(F_B^*/F_d)^{\eta/\eta^* - 1}$. With $\eta/\eta^* = 5$, we therefore expect rolling at η^* for $\epsilon_0 > \epsilon_0^{firm}(\eta^*) \approx 15\epsilon_0^{firm}(\eta = 5\eta^*)$. A factor of roughly this order of magnitude between the off rates at the border between rolling and firm adhesion for $\eta = 5$ mPa s and $\eta^* = 1$ mPa s can also be read off from Fig. 9(a). On the other

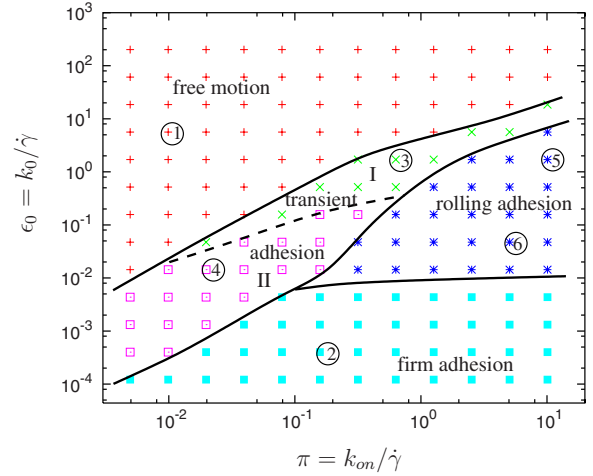


FIG. 8. (Color online) The on-off state diagram displays different stationary states of leukocyte motion obtained by simulations. The ordinate shows the dimensionless unstressed off rate ϵ_0 , the horizontal axis the dimensionless on rate π . Snapshots for the cell velocities at the (π, ϵ_0) parameter values marked by numbered circles are shown in Fig. 7: numbered circle 1, Fig. 7(a); numbered circle 2, Fig. 7(b); numbered circle 3, Fig. 7(c); numbered circle 4, Fig. 7(d); numbered circle 5, Fig. 7(e); numbered circle 6, Fig. 7(f). Parameters used are the same as for Fig. 6.

hand no essential shift in the borderline between the states rolling and the “transient I” can be spotted when the viscosity is changed. This is the case as the referred line occurs at rather large ϵ_0 values at which ϵ_0 appears to dominate over the force (viscosity) dependent part in the Bell equation for the total off rate ϵ . These estimates suggest that the rolling state disappears at even smaller viscosities (one or two magnitudes smaller than that of water) than used in Fig. 9(a). This is indeed observed for simulations in this viscosity range (data not shown). Note however that in this range, the assumption of small Reynolds number might fail.

B. Bond spring constant

Figure 9(b) shows the state diagrams for three different spring constants $\kappa_{stiff}, \kappa_{int}, \kappa_{soft} = 5 \times 10^{-2}, 5 \times 10^{-3}, 5 \times 10^{-5}$ N/m, respectively. The intermediate spring constant κ_{int} is of the same order of magnitude as the spring constant of the P-selectin and its ligand bond [48]. The softest spring constant κ_{soft} mimics the effect of soft microvilli [49]. From Fig. 9(b) we first notice that the firm adhesion state for κ_{stiff} occurs at smaller off rates ϵ_0 for small on rates π and at larger off rates for large on rates compared to the case of the intermediate spring constant κ_{int} . A closer view identifies two effects that are responsible for this observation at small on rates. First, the stiffness of the bond results in a small elongation which then leads to an obtuse bond-wall angle (the angle χ in Fig. 4). The more obtuse this angle is, the more the bond must be loaded to compensate the shear force. In addition, the transport of the cell and thus also the bond extension is governed by the shear rate $\dot{\gamma}$. A stiffer bond is therefore loaded faster. Both the faster loading [59] and the larger bond force result in an effective increase of the off rate

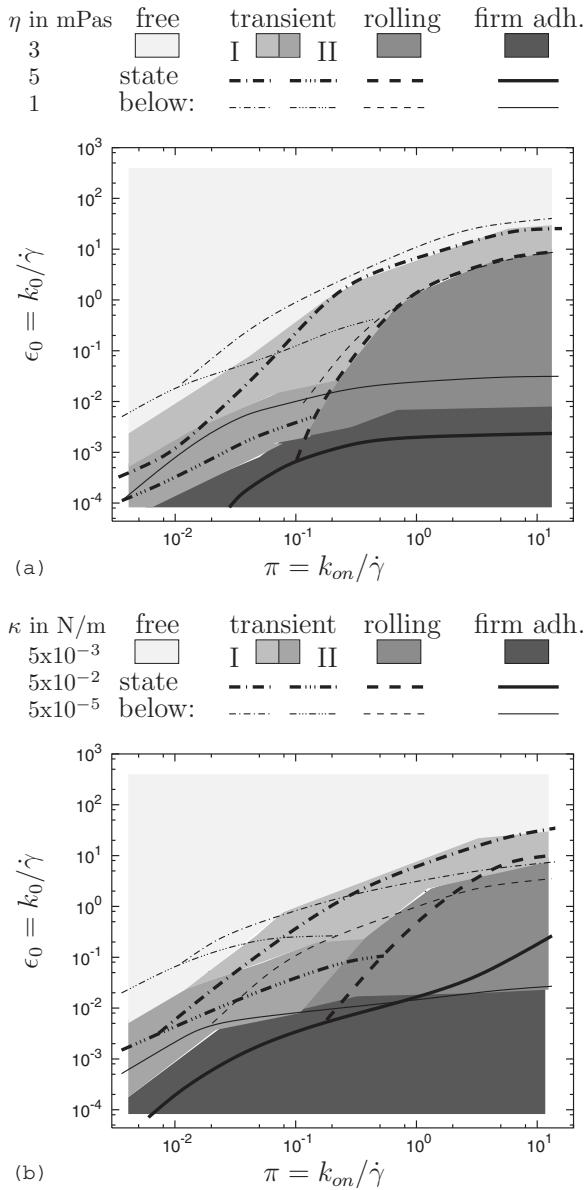


FIG. 9. (a) On-off state diagrams for different viscosities η . The filled areas define the states of motion as determined from simulations at a reference viscosity $\eta = 3$ mPa s. The lines denote the borders between the states of motion at a lower and at a higher viscosity than the reference viscosity. The thin (thick) lines refer to a viscosity $\eta = 1$ mPa s (5 mPa s). The figure legend tells which state is found below the corresponding line. (b) States of motion at different spring constants κ . The filled areas are the states of motion for the intermediate spring constant $\kappa = 5 \times 10^{-3}$ N/m. The thin (thick) lines refer to $\kappa = 5 \times 10^{-5}$ N/m ($\kappa = 5 \times 10^{-3}$ N/m). [Other parameters used for simulations in both (a) and (b): Number of receptors $N_r = 2500$, ligand-ligand distance $d = 2.5 \times 10^{-2} R$, in (a): $\kappa = 5 \times 10^{-3}$ N/m; in (b): $\eta = 1$ mPa s.]

ϵ , which at small on rates can be compensated by smaller off rates ϵ_0 . In contrast, at larger on rates the fast dissociation is compensated by fast binding of new bonds and rebinding of just dissociated bonds. Therefore, the increase in the effective ϵ plays a minor role. On the other hand the faster loading leads to a faster stop of the cell, so that to maintain rolling

even larger rates ϵ_0 are necessary in this range of π .

When we compare the intermediate spring constant κ_{int} with the soft one κ_{soft} , we see that the region of rolling shrinks for the soft case. In the case of the soft spring constant at larger π rolling turns into “transient I” already at smaller off rates ϵ_0 . In addition, rolling occurs still at much smaller on rates than in the case of κ_{int} and κ_{stiff} , respectively. Both of these observations have their origin in the larger tether elongation that is possible for soft bonds. This elongation effectively increases the contact area (i.e., the area on the cell surface that is less than the capture length r_0 away from the wall). More precisely, bonds can still only be formed within the contact region but can then exist also outside the contact region. If the off rate ϵ_0 is not too large, this effect leads to an effective increase in the number of available receptors, which explains the rolling in the region of smaller π . For larger ϵ_0 bonds rupture quickly also at small bond forces. In the case of soft bonds the bond force is then not sufficiently high as to reduce the translational velocity to induce rolling. The state of motion then rather appears to be transient I or free motion.

C. Receptor number

Before discussing the impact of the number of receptor patches on the cell surface, we first estimate the number of receptor patches within the contact zone given N_r . Supposing the cell touches the wall it immediately follows from basic geometrical considerations that on average $N_{r,contact} = N_r r_0/2$ receptor patches are in principle in capture range to wall ligands. On the other hand, the average number of ligands in range to receptors is calculated from the product of the projected area of the contact zone to the wall and the ligand density. The radius of the projected contact area is $\approx \sqrt{2Rr_0}$ as $r_0 \ll R$. Thus the number of ligands in the contact zone is $N_{l,contact} = 2\pi Rr_0/d^2$.

In Fig. 10(a) we have $N_r = 1000, 2500, 5000$ and $d = 5 \times 10^{-2} R$, i.e., in the contact zone $N_{r,contact} \approx 5, 12.5, 25$ and $N_{l,contact} \approx 25$ (for $r_0 = 0.01R$). Therefore, the number of receptors limits the maximum number of bonds in all three cases. In addition, using as an estimate for the receptor patch density on the sphere $\rho_r = \pi r_0^2 N_r / (4\pi R^2)$, we have $\rho_r \leq 0.125$, i.e., even for $N_r = 5000$ receptor patches, they do not cover the contact zone completely. So, not every receptor necessarily encounters a ligand, and therefore the number of tether bonds is even less than $N_{r,contact}$. In fact, in the rolling state, we actually measure an average number of (1.3–2.6) for $N_r = 1000$, (2–5) for $N_r = 2500$, and (2–6) for $N_r = 5000$ existing bonds, respectively, depending on the actual on and off rate, which is less than the respective $N_{r,contact}$. Figure 10(a) shows that the larger N_r , the smaller on rates π are sufficient to support rolling. Not every receptor-ligand encounter (i.e., overlap of the receptor patch with a ligand) turns into a bond. This happens only with a probability depending on π and the dwelling time of the encounter. Thus, the more encounter occur per time the more bonds will be formed at a given rate π . As the encounter rate increases with increasing number of receptor patches [21], this also increases the average number of bonds.

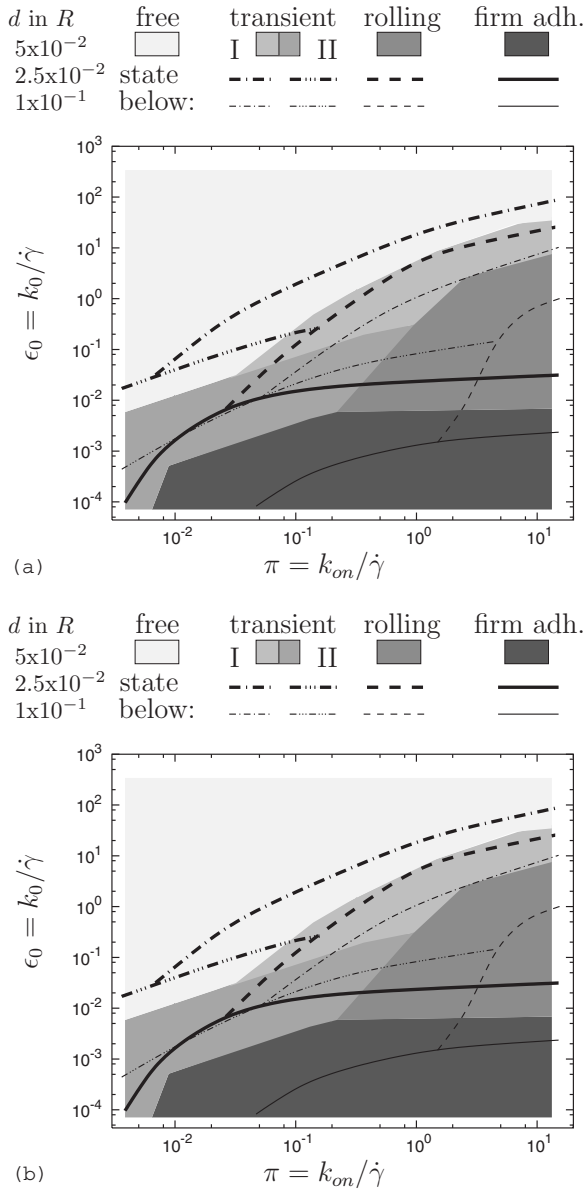


FIG. 10. (a) On-off state diagrams for different numbers of receptors N_r . $N_r=1000$ (thin lines) $N_r=2500$ (filled areas), and $N_r=5000$ (thick lines), ligand-ligand distance $d=5 \times 10^{-2}$, $\kappa=10^{-3}$ N/m, $\eta=1$ mPa s. (b) State diagrams for different ligand-ligand distances $d=1 \times 10^{-1}R$ (thin lines) $d=5 \times 10^{-2}R$ (filled areas) and $d=2.5 \times 10^{-2}R$ (thick lines), number of receptors $N_r=5000$, $\kappa=5 \times 10^{-3}$ N/m, $\eta=1$ mPa s.

Figure 10(a) shows that the transient II region expands with decreasing N_r . The main effect here is that for smaller N_r , the rolling turns into transient motion, while the border line between free and transient motion is much less effected by the decrease in the number of receptor patches. The large (π, ϵ_0) range for the transient states is a signature of few bonds being at work as we will see again when discussing the influence of ligand-ligand distance. Then, single tethers slow the cell down (depending on the off rate they may either arrest the cell some while, resulting in state transient II, or just decelerate them resulting in state transient I), but after dissociation it is unlikely that the current state of motion is

supported by further bonds. However, as long as at least two bonds are possible this effect is partly compensated at large on rates when the probability for receptor-ligand encounter to result in a bond is high.

D. Ligand density

To demonstrate the impact of ligand-ligand distance, Fig. 10(b) shows the state diagrams for $d=10 \times 10^{-2}R$, $5 \times 10^{-2}R$, $2.5 \times 10^{-2}R$, and $N_r=5000$. Using the expressions derived in the previous subsection we now have $N_{l,contact} \approx 6, 25, 100$, respectively, for the number of ligands in the contact zone. The mean number of receptors that may form a bonds is $N_{r,contact}=25$. So, in principle, $N_{r,contact}$ limits the number of bonds in the two cases of higher ligand density and $N_{l,contact}$ is the limiting value only for the very low ligand density. When we measure the average number of bonds at high on rates and relatively small off rates (i.e., in the rolling and firm adhesion region) we find for the intermediate ligand density with $d=5 \times 10^{-2}R$ about five bonds, and for the large ligand density with $d=2.5 \times 10^{-2}R$ about fourteen bonds on average. The later value is slightly larger than $N_{r,contact}=12.5$. This can be explained with the elasticity of the bonds that—once formed—allows them to also exist beyond the contact zone. Thus only at very high ligand densities with $N_{l,contact} \gg N_{r,contact}$, the number of receptors limits the maximum number of bonds. For ligand densities with $N_{l,contact} \gtrsim N_{r,contact}$ a decrease in d still leads to an increase in the average number of bonds as this increases the rate of receptor-ligand encounters.

The basic effect of decreasing the ligand density as illustrated by Fig. 10(b) is the shift of all state from the upper left towards the lower right in the on-off state diagram. For example rolling is only supported at larger on rates and smaller off rates when the ligand density is decreased (i.e., d is increased). Also the border line between the state of free and transient motion is notably shifted between the two extreme cases of ligand density simulated for Fig. 10(b). In fact, the shift of this border line is much more pronounced than in the previous discussed case where the number of receptor patches was reduced. The simple reason for that is that in Fig. 10(a) $N_{r,contact}$ is changed by a factor of 5 whereas in Fig. 10(b) the $N_{l,contact}$ is changed by a factor of almost 20.

Similarly to the case of reduced number of receptor patches, a small ligand density results in an increased (π, ϵ_0) range for transient adhesion. Thus, we note again that at a reduced rate of receptor-ligand encounters, rolling tends to be converted to transient motion. We also note that if several parameters are changed at the same time, the overall effect can be qualitatively understood by superimposing the effects of the single parameter changes described above (data not shown).

E. Application: Experimental determination of the on rate

The on-off state diagrams introduced here display the state of motion of a cell or a receptor covered microbead for a given set of experimental parameters in a wide range of possible on and off rates of the receptor-ligand pair. Because the molecular properties of a given receptor-ligand pair can

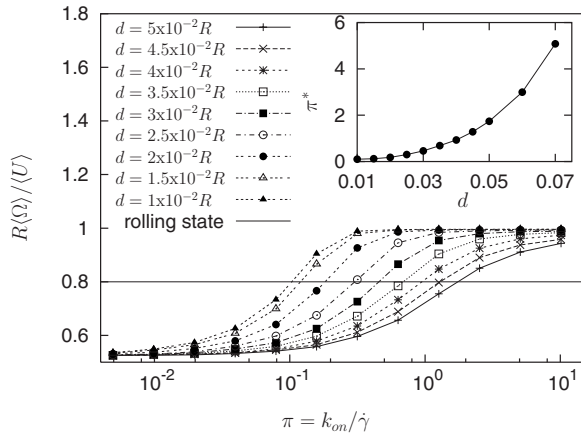


FIG. 11. Determination of the dynamic on rate π from the determination of the state of motion. At the fixed off-rate $\epsilon_0=0.16$, the ratio $R\langle\Omega\rangle/\langle U\rangle$ is plotted as a function of the on rate π for different ligand-to-ligand distances d ranging from $d=1\times 10^{-2}$ to $d=5\times 10^2$. In the π range above the solid line at $R\langle\Omega\rangle/\langle U\rangle=0.8$ the cell is rolling. In the inset the on rate π^* at which $R\langle\Omega\rangle/\langle U\rangle=0.8$ is plotted as a function of d . (Other parameters used: $N_r=2500$, $d=2.5\times 10^{-2}R$, $\dot{\gamma}=100$ Hz, $x_c=2\times 10^{-11}$ m; $\kappa=5\times 10^{-3}$ N/m; $\eta=1$ mPa s.)

be assumed to be given *a priori*, each pair corresponds to one point in the on-off state diagram. In the following we show how the considerations regarding the rolling state presented here can be used to determine the dynamic on rate π of a receptor-ligand pair by changing the external parameter. For this line of reasoning the off rate ϵ_0 is assumed to be known, e.g., from dynamic force spectroscopy experiments. Figure 11 shows the ratio of the mean velocities $R\langle\Omega\rangle/\langle U\rangle$ of the cell as a function of π for different ligand-to-ligand distances d . We see that for a given d the cell is slipping if the on rate is small. Increasing the on rate turns the cell's motion into rolling, i.e., at some critical on rate π^* the ratio $R\langle\Omega\rangle/\langle U\rangle$ reaches the value 0.8 which we defined for rolling. The smaller (larger) the ligand density (ligand-to-ligand distance d) the larger is the critical on rate π^* . More quantitatively this is shown in the inset of Fig. 11 where π^* is plotted as a function of d . If one now changes the ligand density in a series of flow chamber experiments from low to high values and by doing so determines the d value at which the motion of the cell turns from transient to rolling motion, then one can read from the inset of Fig. 11 the on rate π of the receptor-ligand bond.

The described procedure does not work for very small on rates for which rolling is not possible even for very large ligand densities (i.e., $d\ll r_0$). On the other hand one can always find a ligand distance at which rolling is not possible whatever value the on rate takes. At very low ligand densities $d\gg r_0$ the reaction is limited by the encounter rate and even for very large rates π rolling is not possible.

V. DISCUSSION

In this paper we introduced a version of the adhesive dynamics algorithm. In contrast to earlier work, our approach

also includes the diffusive motion of cells resulting from thermal fluctuations. This allowed us to spatially resolve receptors and ligands. An immediate advantage of this approach is that the single bond on rate k_{on} can be chosen to be independent of the relative motion of cell and substrate. In this work, we focused on the different dynamic states of motion which can be identified on the cellular level. We first noticed that the action of a single bond not only slows the cell down, but also changes the motion from slipping (which is the case for cells moving free in hydrodynamic flow) to rolling in the sense $R\langle\Omega\rangle/\langle U\rangle\rightarrow 1$. In the case of multiple bonds, rolling can also be observed regarding the mean values of the velocities, i.e., $R\langle\Omega\rangle/\langle U\rangle\rightarrow 1$ at proper rates of bond formation and rupturing. This motivated us to define the state of rolling adhesion as $R\langle\Omega\rangle/\langle U\rangle>0.8$. By extending these observations we defined five distinct states of stationary cell motion. These states were then displayed in so-called on-off state diagrams which showed the impact of different molecular rates. In addition, we investigated the effect of external parameters. For example, we showed that the cellular motion is changed considerably when the viscosity of the medium is changed.

Our work shows that different dynamic states of cell motion can be defined in a systematic and quantitative way. In particular, calculations of state diagrams allow us to obtain a complete understanding of the way molecular and other parameters determine motion on the scale of a cell. Similar approaches have been taken before [57,58], but without a proper definition of rolling in the mechanical sense. Our computer work now shows that including the rotational degrees of freedom allows us to investigate the transition from hydrodynamic slipping to bond-mediated rolling in a more detailed way. Experimentally it is certainly a challenge to obtain similar data in flow chamber experiments for micron-sized beads or cells. In principle, making use of recent nanotechnological developments one could attach receptors to micron-sized beads which are covered with anisotropic surface layers [60,61]. If these layers are anisotropically reflective, rotational motion of the spheres can be recorded. For cells, one would have to track surface or intracellular markers (e.g., mitochondria or nuclei).

We also suggested a procedure to experimentally determine values for on rates from monitoring cell motion (cf. Sec. IV E). In contrast to the off rate, which can be measured, e.g., from dynamic force spectroscopy experiments, it is very difficult to infer values for the on rate k_{on} in cell adhesion, where both partners have to be attached to appropriate surfaces. Here, also one could make use of recent developments in nanotechnology. As we have shown above, the ligand-to-ligand distance d is a crucial control parameter in our system. Recently, it has become possible to control this parameter using nanopatterend and biofunctionalized arrays of gold dots [62]. Therefore, in the future our predictions regarding the effect of ligand positioning might be compared directly to experimental data, especially if compared with a measurement of the rotational degrees of freedom.

For conceptual and computational simplicity, here we have used the Bell model for the force dependence of the off-rate k_{off} . In principle, it would be easy to include more complicated rupture scenarios, such as the catch-slip behav-

ior recently reported for both P - and L -selectin [7,15]. There is good reason to believe that this molecular behavior is essential for the physiological function of these molecules and different theoretical models have been suggested to explain this behavior [63–65]. If combined with our modeling framework for adhesive dynamics, these models might be tested against experimental data from flow chamber experiments. Such an approach would have the big advantage that it avoids testing single molecules outside their physiological environment, which is especially problematic for adhesion receptors which usually are embedded in the plasma membrane and regulated by the cytoskeleton.

Further possible extensions of our simulation framework include models for cell deformability and hydrodynamic interactions between cells. Cell deformations in free flow should become relevant only at shear rates well above 100 Hz [22]. In adhesion, cell deformation depends also on the number and strength of adhesion bonds. In the case of strong adhesion, it is well known that also viscoelastic changes occur, including elongation of microvilli [49]. For computational and conceptual simplicity, here we have focused on the case of moderate shear flow and adhesion, when the effect of cell deformability is small. Moreover deformations are irrelevant for rigid microbeads, which have been shown to result in similar physical effects as described for cellular systems [11–13]. In order to combine elastic effects and hydrodynamics, a very powerful framework is provided by multiparticle collision dynamics [66], which in principle also would allow one to include nonlaminar flow conditions and hydrodynamic interactions between cells. However, these effects can be safely avoided in flow chamber experiments by using sufficiently small shear rates and cell numbers. As explained above, an elegant way to test our theoretical predictions experimentally would be the combination of appropriately coated microbeads with nanostructured substrates.

Finally we comment on the applicability of our approach to other systems that are based on the stochastic interplay between transport and adhesion. In the work presented here, we have considered a situation where receptor and ligands are both tethered to macroscopic surfaces. However, similar physical processes are relevant if the two molecular binding partners are free in solution, for example in affinity measurements [67] or shear-induced adhesion of blood-clotting factors [68]. Another biological system for which the concepts for bond formation, bond rupture, and transport discussed here can be applied is the cargo transport by multiple molecular motors [69,70]. Compared with rolling adhesion, the cell is replaced by the cargo (e.g., a vesicle), the cell-anchored receptors by molecular motors, and the substrate-anchored ligands by binding sites on the filament. In contrast to the case of rolling adhesion, now the system is not driven by some external force, but the molecular motors actively step forward and pull their cargo against an external viscous friction force. Our approach can also be applied to nonbiological systems. For example, it is well known that erratic motion also occurs in the context of sliding friction. A flat slider that is pulled above a plain wall exhibits stick-slip motion in some range of the pulling velocity. It was shown recently that this special kind of motion can be explained

assuming the stochastic formation and rupture of molecular bonds between the slider and the wall [71]. Thus the stick-slip motion of sliding friction and the erratic movement of cells in rolling adhesions seem to be based on the similar physical principles.

ACKNOWLEDGMENTS

This work was supported by the Center for Modeling and Simulation in the Biosciences (BIOMS) and the Cluster of Excellence *CellNetworks* at Heidelberg. Additional support came from the Minerva Foundation through a research grant for C.B.K. We thank Ronen Alon and the members of his group for many interesting discussions on rolling adhesion.

APPENDIX: BOND DYNAMICS ALGORITHM

The sphere's motion is described by Eq. (3). If no bond between the sphere receptors and wall ligands exists, we take for the direct force \mathbf{F}^D only gravity into account, i.e., the six-dimensional force and torque vector is given by $\mathbf{F}^D = (-\Delta mg \mathbf{e}_z, \mathbf{0})$ with g the earth acceleration constant. Receptor-ligand bonds lead to additional contributions to both the force and momentum part of \mathbf{F}^D . More precisely, a bond between a ligand located at \mathbf{r}_l and a receptor located at \mathbf{r}_r on the sphere's surface (see Fig. 1) pulls with a force

$$\mathbf{F}_B = \hat{\mathbf{r}}_b F(r_b), \quad \hat{\mathbf{r}}_b := \frac{\mathbf{r}_l - \mathbf{r}_r}{\|\mathbf{r}_l - \mathbf{r}_r\|}, \quad r_b := \|\mathbf{r}_l - \mathbf{r}_r\|. \quad (\text{A1})$$

$F(x)$ is the force extension curve that describes by what force the bond must be pulled to stretch it up to a total length x . Here, we consider the bonds to be semiharmonic springs (cable model)

$$F(x) = \kappa(x - l_0)\Theta(x - l_0), \quad \Theta(x) := \begin{cases} 1, & x > 0, \\ 0, & \text{else,} \end{cases} \quad (\text{A2})$$

with l_0 the resting length and κ the spring constant. The cable model is the simplest model for polymeric tethers. In the cable model a bond behaves as a spring only if it is stretched (extension larger than the resting length), otherwise the bond exerts no force on the sphere. Treating the receptor-ligand complex as a harmonic spring works fine in the small extension regime [48]. For large extensions the force extension curve for polymers is supposed to grow much faster than linear, and when the bond extension approaches the total contour length of the receptor-ligand complex it even diverges (strain stiffening). However, typical bonds are weak and their rupture probability increases exponentially with force. Therefore, we expect bond extensions to be restricted to the linear regime. As the bond force pulls on the sphere's surface also a torque results

$$\mathbf{T}_B = \hat{\mathbf{r}} \times \mathbf{F}_B(\mathbf{r}_b),$$

where $\hat{\mathbf{r}}$ is the connection vector from the center of the sphere to the point on its surface where the receptor is attached (see Fig. 4). Thus, the total force and torque contribution to \mathbf{F}^D by the bonds is

$$\kappa \sum_{i=1}^{N_r} q_i F(r_b^i) (\hat{\mathbf{r}}_b^i \hat{\mathbf{r}}^i \times \hat{\mathbf{r}}_b^i), \quad (\text{A3})$$

with N_r the total number of receptors and $q_i=1$ if the i th receptor forms a bond and zero otherwise. The $q_i, i=1, \dots, N_r$ are stochastic variables. Thus, the contribution, Eq. (A3), lets the direct force \mathbf{F}^D also become a stochastic variable.

With this at hand we can now define the *adhesive dynamics* rules, applied in each update step Δt (cf. Fig. 1):

(i) The sphere's position and orientation is updated according to Eq. (3) (for an explicit description see Ref. [22]).

(ii) The receptor positions in the flow chamber coordinate system are calculated.

(iii) Each inactive receptor is represented by a capture ball with radius $r_0 \ll 1$.

(iv) If the distance between a receptor and any ligand is $\leq r_0$ a bond is established with probability $p_{on}=1-\exp(-\Delta t k_{on})$, then the resting length of the bond is set to the receptor-ligand distance at the instance of bond formation (i.e., the bond force at the moment of bond formation is zero)

and is stored together with the ligand position. A bond can only be formed if the corresponding receptor and ligand are not already part of another bond.

(v) For each active bond, the contribution to \mathbf{F}^D is calculated.

(vi) Each existing bond dissociates with a rate given by the Bell equation, Eq. (5). Thus, each bond ruptures with probability $p_{off}=1-\exp[-\Delta t k_{off}(F)]$, where F is the instantaneous force acting along this bond.

When a bond has ruptured, both the receptor and the ligand can form a new bond in the next time step according to the rule (iv). As for the resting length l_0 of a bond always $l_0 < r_0 \ll 1$ is true, modeling bonds as harmonic springs in both the extension and compression regime would not make much difference to the results that are obtained by the cable model. Given the probability for bond formation or rupture p_{on} or p_{off} , respectively, a standard Monte Carlo technique is used to decide whether the action happens or not: Using a pseudorandom number generator a random number *rand* from the uniform distribution in the interval $[0,1]$ is drawn. If then $p_{on/off} > \text{rand}$ the respective action takes place, otherwise not.

-
- [1] T. A. Springer, *Cell* **76**, 301 (1994).
 [2] H. Rossiter, R. Alon, and T. S. Kupper, *Mol. Med. Today* **3**, 214 (1997).
 [3] R. Alon and M. L. Dustin, *Immunity* **26**, 17 (2007).
 [4] M. B. Lawrence and T. A. Springer, *Cell* **65**, 859 (1991).
 [5] R. Alon, D. A. Hammer, and T. A. Springer, *Nature (London)* **374**, 539 (1995).
 [6] R. Alon, S. Chen, K. D. Puri, E. B. Finger, and T. A. Springer, *J. Cell Biol.* **138**, 1169 (1997).
 [7] B. T. Marshall, M. Long, J. W. Piper, T. Yago, R. P. McEver, and C. Zhu, *Nature (London)* **423**, 190 (2003).
 [8] J. Lou, T. Yago, A. G. Klopocki, P. Mehta, W. Chen, V. I. Zarnitsyna, N. V. Bovin, C. Zhu, and R. P. McEver, *J. Cell Biol.* **174**, 1107 (2006).
 [9] E. B. Finger, K. D. Puri, R. Alon, M. B. Lawrence, U. H. von Andrian, and T. A. Springer, *Nature (London)* **379**, 266 (1996).
 [10] U. S. Schwarz and R. Alon, *Proc. Natl. Acad. Sci. U.S.A.* **101**, 6940 (2004).
 [11] T. Yago, V. I. Zarnitsyna, A. G. Klopocki, R. P. McEver, and C. Zhu, *Biophys. J.* **92**, 330 (2007).
 [12] D. K. Brunk, D. J. Goetz, and D. A. Hammer, *Biophys. J.* **71**, 2902 (1996).
 [13] A. W. Greenberg, D. K. Brunk, and D. A. Hammer, *Biophys. J.* **79**, 2391 (2000).
 [14] S. Chen and T. A. Springer, *Proc. Natl. Acad. Sci. U.S.A.* **98**, 950 (2001).
 [15] T. Yago, J. Wu, C. D. Wey, A. G. Klopocki, C. Zhu, and R. P. McEver, *J. Cell Biol.* **166**, 913 (2004).
 [16] R. Shamri, V. Grabovsky, J.-M. Gauguier, S. Feigelson, E. Manevich, W. Kolanus, M. K. Robinson, D. E. Staunton, U. H. von Andrian, and R. Alon, *Nat. Rev. Immun.* **6**, 497 (2005).
 [17] G. I. Bell, *Science* **200**, 618 (1978).
 [18] D. A. Hammer and S. M. Apte, *Biophys. J.* **63**, 35 (1992).
 [19] S. K. Bhatia, M. R. King, and D. A. Hammer, *Biophys. J.* **84**, 2671 (2003).
 [20] K. E. Caputo, D. Lee, M. R. King, and D. A. Hammer, *Biophys. J.* **92**, 787 (2007).
 [21] C. Korn and U. S. Schwarz, *Phys. Rev. Lett.* **97**, 138103 (2006).
 [22] C. B. Korn and U. S. Schwarz, *J. Chem. Phys.* **126**, 095103 (2007).
 [23] *Modeling and Simulation of Capsules and Biological Cells*, edited by C. Pozrikidis (Chapman & Hall/CRC Press, Boca Raton, FL, 2003).
 [24] N. A. N'Dri, W. Shyy, and R. Tran-Son-Tay, *Biophys. J.* **85**, 2273 (2003).
 [25] D. B. Khismatullin and G. A. Truskey, *Phys. Fluids* **17**, 031505 (2005).
 [26] S. Jadhav, C. D. Eggleton, and K. Konstantopoulos, *Biophys. J.* **88**, 96 (2005).
 [27] A. Alexeev, R. Verberg, and A. C. Balazs, *Soft Matter* **2**, 499 (2006).
 [28] C. Sun and L. L. Munn, *Biophys. J.* **88**, 1635 (2005).
 [29] M. R. King, S. D. Rodgers, and D. A. Hammer, *Langmuir* **17**, 4139 (2001).
 [30] K.-C. Chang, D. F. J. Tees, and D. A. Hammer, *Proc. Natl. Acad. Sci. U.S.A.* **97**, 11262 (2000).
 [31] K. E. Caputo and D. A. Hammer, *Biophys. J.* **89**, 187 (2005).
 [32] J. F. Brady and G. Bossis, *Annu. Rev. Fluid Mech.* **20**, 111 (1988).
 [33] B. Cichocki and R. B. Jones, *Physica A* **258**, 273 (1998).
 [34] J. Honerkamp, *Stochastic Dynamical Systems* (VCH Publishers, Zurich, 1994).
 [35] C. W. Gardiner, *Handbook of Stochastic Methods* (Springer-Verlag, Berlin, 1985).

- [36] D. L. Ermak and J. A. McCammon, *J. Chem. Phys.* **69**, 1352 (1978).
- [37] C. Korn, Ph.D. thesis, Potsdam University, 2007.
- [38] G. S. Perkins and R. B. Jones, *Physica A* **189**, 447 (1992).
- [39] A. J. Goldman, R. G. Cox, and H. Brenner, *Chem. Eng. Sci.* **22**, 653 (1967).
- [40] H. C. Berg and E. M. Purcell, *Biophys. J.* **20**, 193 (1977).
- [41] H. A. Kramers, *Physica (Amsterdam)* **7**, 284 (1940).
- [42] E. Evans and K. Ritchie, *Biophys. J.* **72**, 1541 (1997).
- [43] E. A. Evans and D. A. Calderwood, *Science* **316**, 1148 (2007).
- [44] J. Shillcock and U. Seifert, *Phys. Rev. E* **57**, 7301 (1998).
- [45] K.-C. Chang and D. A. Hammer, *Biophys. J.* **76**, 1280 (1999).
- [46] H. P. Ting-Beall, D. Needham, and R. M. Hochmuth, *Blood* **81**, 2774 (1993).
- [47] L. L. Munn, R. J. Melder, and R. K. Jain, *Biophys. J.* **67**, 889 (1994).
- [48] J. Fritz, A. G. Katopodis, F. Kolbinger, and D. Anselmetti, *Proc. Natl. Acad. Sci. U.S.A.* **95**, 12283 (1998).
- [49] J.-Y. Shao, H. P. Ting-Beall, and R. M. Hochmuth, *Proc. Natl. Acad. Sci. U.S.A.* **95**, 6797 (1998).
- [50] O. Dwir, A. Solomon, S. Mangan, G. S. Kansas, U. S. Schwarz, and R. Alon, *J. Cell Biol.* **163**, 649 (2003).
- [51] S. Knutton, M. C. B. Sumner, and C. A. Pasternak, *J. Cell Biol.* **66**, 568 (1975).
- [52] S. Chen and T. A. Springer, *J. Cell Biol.* **144**, 185 (1999).
- [53] G. I. Bell, M. Dembo, and P. Bongrand, *Biophys. J.* **45**, 1051 (1984).
- [54] K. L. Moore, K. D. Patel, R. E. Bruehl, L. Fugang, D. A. Johnson, H. S. Lichenstein, R. D. Cummings, D. F. Bainton, and R. P. McEver, *J. Cell Biol.* **128**, 661 (1995).
- [55] K. D. Patel, M. U. Nollert, and R. P. McEver, *J. Cell Biol.* **131**, 1893 (1995).
- [56] W. Hortshemke and R. Lefever, *Noise-Induced Transitions* (Springer-Verlag, Berlin, 1984).
- [57] E. F. Krasik and D. A. Hammer, *Biophys. J.* **87**, 2919 (2004).
- [58] R. Bruinsma, in *Physics of Biomaterials: Fluctuations, Self-assembly and Evolution*, edited by T. Riste and D. Sherrington (Kluwer Academic, Norwell, MA, 1996), pp. 61–101.
- [59] T. Erdmann and U. S. Schwarz, *Europhys. Lett.* **66**, 603 (2004).
- [60] F. Burmeister, C. Schäfle, B. Keilhofer, C. Bechinger, J. Boneberg, and P. Leiderer, *Adv. Mater. (Weinheim, Ger.)* **10**, 495 (1998).
- [61] M. Albrecht, G. Hu, I. L. Guhr, T. C. Ulbrich, J. Boneberg, P. Leiderer, and G. Schatz, *Nat. Mater.* **4**, 203 (2005).
- [62] M. Arnold, E. A. Cavalcanti-Adam, R. Glass, J. Blümmel, W. Eck, M. Kantlehner, H. Kessler, and J. P. Spatz, *ChemPhysChem* **5**, 383 (2004).
- [63] E. Evans, A. Leung, V. Heinrich, and C. Zhu, *Proc. Natl. Acad. Sci. U.S.A.* **101**, 11281 (2004).
- [64] W. Thomas, M. Forero, O. Yakovenko, L. Nilsson, P. Vicini, E. Sokurenko, and V. Vogel, *Biophys. J.* **90**, 753 (2006).
- [65] Y. V. Pereverzev and O. V. Prezhdo, *Phys. Rev. E* **73**, 050902(R) (2006).
- [66] H. Noguchi and G. Gompper, *Proc. Natl. Acad. Sci. U.S.A.* **102**, 14159 (2005).
- [67] C. Wofsy and B. Goldstein, *Biophys. J.* **82**, 1743 (2002).
- [68] S. W. Schneider, S. Nuschele, A. Wixforth, C. Gorzelanny, A. Alexander-Katz, R. R. Netz, and M. F. Schneider, *Proc. Natl. Acad. Sci. U.S.A.* **104**, 7899 (2007).
- [69] S. Klumpp and R. Lipowsky, *Proc. Natl. Acad. Sci. U.S.A.* **102**, 17284 (2005).
- [70] J. Beeg, S. Klumpp, R. Dimova, R. Serral Gracià, E. Unger, and R. Lipowsky, *Biophys. J.* **94**, 532 (2008).
- [71] A. E. Filippov, J. Klafter, and M. Urbakh, *Phys. Rev. Lett.* **92**, 135503 (2004).